

# Breakdown of the static picture of defect energetics in halide perovskites: the case of the Br vacancy in CsPbBr<sub>3</sub>

Ayala V. Cohen,<sup>1</sup> David A. Egger,<sup>2</sup> Andrew M. Rappe,<sup>3</sup> and Leeor Kronik<sup>1</sup>

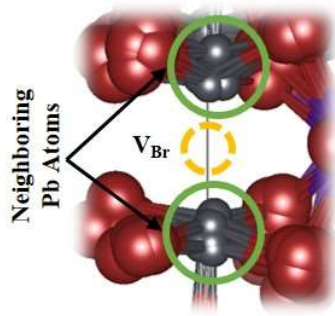
<sup>1</sup> *Department of Materials and Interfaces, Weizmann Institute of Science, Rehovoth 76100, Israel.*

<sup>2</sup> *Institute of Theoretical Physics, University of Regensburg, 93040 Regensburg, Germany.*

<sup>3</sup> *Department of Chemistry, University of Pennsylvania, Philadelphia, PA 19104–6323, USA.*

## Abstract

We consider the Br vacancy in CsPbBr<sub>3</sub> as a prototype for the impact of structural dynamics on defect energetics in halide perovskites (HaPs). Using first-principles molecular dynamics based on density functional theory, we find that the static picture of defect energetics breaks down; the energy of the V<sub>Br</sub> level is found to be intrinsically dynamic, oscillating by as much as 1 eV on the ps time scale at room temperature. These significant energy fluctuations are correlated with the distance between the neighboring Pb atoms across the vacancy and with the electrostatic potential at their atomic sites. The unusually strong coupling of structural dynamics and defect energetics bears important implications for both experimental and theoretical analysis of defect characteristics in HaPs and may hold significant ramifications for carrier transport and defect tolerance in this class of photovoltaic materials.



Halide perovskites (HaPs) have emerged as remarkably efficient materials for optoelectronic applications, notably for photovoltaics, but also for light emitting diodes and other devices.<sup>1-8</sup> One of the most intriguing features of HaPs is the very long lifetime of photoexcited carriers (up to several  $\mu\text{s}$ ),<sup>9-11</sup> which is essential for key device parameters, *e.g.*, the open-circuit voltage of HaP-based photovoltaic cells.<sup>12</sup> These long lifetimes are particularly remarkable given that HaP compounds are typically fabricated using relatively low-energy, solution-based material syntheses.<sup>13-16</sup> This suggests that electronic defect states in these materials are unusually benign electrically.<sup>11,17-21</sup> Therefore, there are significant and on-going efforts to understand defect energetics and its relation to charge carrier scattering and recombination in HaP materials.

Recently, a large number of theoretical investigations have examined the microscopic origins and energetics of intrinsic defects in HaPs, mostly using density functional theory (DFT).<sup>22-43</sup> While these studies exhibit scatter in the results owing to the type of approximate density functional used, as well as various numerical and convergence issues, they do share one key common element, which is the adoption of a static scenario. In other words, these studies allow the surrounding nuclei to adapt to the presence of a defect via a well-defined local minimum in the potential energy surface, and therefore tacitly assume that dynamic nuclear effects are of secondary importance. Comparison between theory and experiment shows this assumption to be justified in a wide range of semiconductors of scientific and technological interest.<sup>44</sup> However, it is by now apparent that HaPs do not behave as ordinary semiconductors in terms of lattice dynamics. They are mechanically much softer than other efficient optoelectronic materials<sup>21,45-51</sup> and exhibit unusual structural dynamical phenomena including large-amplitude, anharmonic nuclear fluctuations and dynamic symmetry breaking, even at room temperature (RT).<sup>21,48,52-73</sup> Given that such phenomena surely modulate the energy landscape both spatially and temporally, one may ask whether the assumption of a static defect is valid, and if not, what are the consequences of its breakdown.

Here, we address this question by performing first principles molecular dynamics (MD) calculations, based on DFT, which allow us to study point defect properties while fully accounting for structural dynamics. As an illuminating test case, we focus on  $\text{CsPbBr}_3$ , which is known to exhibit structural dynamics on par with those of hybrid organic-inorganic HaPs,<sup>57</sup> and examine the abundant halide vacancy therein.<sup>34,36</sup> We

find significant temporal variations in defect energies, which are strongly correlated with nuclear dynamics, thereby precluding the assignment of a unique defect energy level. This suggests a breakdown of the static picture, with possible repercussions for material and device behavior.

All DFT-based MD calculations were performed using the Perdew-Burke-Ernzerhof (PBE)<sup>74</sup> form of the generalized-gradient approximation, augmented by dispersion terms calculated within the Tkatchenko-Scheffler (TS) scheme<sup>75</sup> using an iterative Hirshfeld partitioning of the self-consistently computed charge density.<sup>76</sup> This approach has previously been found to be highly useful for an accurate description of the structure and energetics of ionic compounds with components of dispersive binding.<sup>76,77</sup> We note that the Heyd-Scuseria-Ernzerhof (HSE)<sup>78</sup> short-range hybrid functional, together with the inclusion of spin-orbit coupling (SOC) effects, has previously been shown to be more accurate in predicting defect energetics in HaPs.<sup>26</sup> However, a comprehensive MD analysis of the system studied here based on HSE+SOC is at present prohibitive computationally. Here, our interest is not in the absolute defect level position, but rather in its thermal fluctuations. As shown in the supporting information (SI), Section 1, all fluctuation trends reported below are fully reproduced by HSE+SOC calculations performed for selected points in the MD run, thus validating the use of PBE level calculations in this case. All calculations were performed using the Vienna ab initio simulation package (VASP),<sup>79</sup> a plane-wave basis code in which ionic cores are described by the projected augmented wave (PAW)<sup>80</sup> method. A plane-wave cutoff of 300 eV and a  $10^{-4}$  eV/supercell convergence criterion for the total energy were used in all HaP calculations.

All first-principles MD simulations of CsPbBr<sub>3</sub> in its RT orthorhombic phase were based on previously used cell parameters ( $a=8.18\text{\AA}$ ,  $b=11.64\text{\AA}$ ,  $c=8.13\text{\AA}$ ),<sup>57</sup> obtained from a PBE+TS calculation. Whereas PBE overestimates cell parameters, the inclusion of dispersive terms greatly improves the agreement between experimental and theoretical lattice parameters,<sup>81-84</sup> in our case to within  $\sim 0.8\%$  of the reported experimental values.<sup>85</sup> A  $2\times 2\times 2$  supercell (containing 160 atoms) was employed, and a single Br vacancy ( $V_{\text{Br}}$ ) was introduced. Owing to the size of this supercell,  $\Gamma$ -point only sampling of the Brillouin zone was found to be sufficient for differences in defect state eigenvalues. The DFT-MD calculations were performed using a Nosé-Hoover thermostat<sup>86,87</sup> with the temperature set to 298 K, and a Verlet algorithm to integrate

the nuclear equations of motion, using a timestep of 10 fs, previously found to be sufficient for MD of CsPbBr<sub>3</sub>.<sup>57</sup> To ascertain the suitability of this time step, we repeated the MD run of the defect-containing supercell with a significantly smaller time step of 2 fs. The results of this comparison, given in Section 2 of the SI, establish that the two time steps results in similar statistics. CsPbBr<sub>3</sub> was thermally equilibrated, followed by 60 ps of RT dynamics. For comparison, similar MD calculations have been performed for the well-known As<sub>Ga</sub> anti-site defect in GaAs, using a 3×3×3 GaAs supercell, which maintains a similar defect-defect image distance as in the HaP supercell, with all other parameters being the same except for a slightly larger cutoff energy of 350 eV. Additional tests of the effects of denser *k*-grids, of spin-polarization, and of supercell size (defect density and image interaction), are presented in Sections 3 and 4 of the SI.

The standard approach to computing defect level energetics is to consider the cross-over point in the formation energy of the relaxed defect at different charge states.<sup>44</sup> Because our MD data inherently and purposefully produce unrelaxed geometries, we focus instead on the instantaneous eigenvalue of the defect state as a proxy to its instantaneous charge transition level. We are well aware that Kohn-Sham eigenvalues are not charge transition levels, but we also emphasize that the two are qualitatively and often semi-quantitatively related.<sup>88</sup> Furthermore, in the SI, Section 5, we show for the last 15 ps of the MD run that trends in the fluctuation of the eigenvalues and of optical (unrelaxed) transition energies are similar. For simplicity and clarity, all further mentions of the term “defect level” in this paper refer to the Kohn-Sham eigenvalue related to the defect state.

Fig. 1a shows the temporal evolution of three key eigenvalues in the CsPbBr<sub>3</sub> supercell containing a neutral V<sub>Br</sub> defect: the conduction band minimum (CBM), the valence band maximum (VBM), and the defect-related eigenvalue. The energy variations of the VBM and CBM energies over the last 30 ps of the MD simulation are found to be ≈0.2-0.3 eV. They are uncorrelated, leading to fluctuations of ≈0.4 eV in the band gap of the material, a result that is consistent with prior studies.<sup>65,66,89</sup> Also consistent with prior studies is the fact that the fluctuations of these bulk properties somewhat diminish further with supercell size, but remain finite<sup>90</sup> (See SI, section 4, for more details). In stark contrast, the temporal fluctuations of the V<sub>Br</sub>-related defect energy level, and more importantly, the fluctuations in the distance of this level from

the conduction band edge, are much larger, and are much more weakly affected by an increase in supercell size due to the localization of the defect. They can be as large as  $\approx 1$  eV (see Table 1 for detailed statistics), often on a time scale  $< 1$  ps. As a consequence, the defect level spans a surprisingly wide energy range, from almost midgap to almost the CBM! For comparison, Fig. 1b shows the results of analogous calculations of the same three eigenvalues for a GaAs supercell containing a neutral  $\text{As}_{\text{Ga}}$  defect. The fluctuations in the band edge energies are smaller ( $\approx 0.1$ - $0.2$  eV) than in  $\text{CsPbBr}_3$ , but more importantly, the fluctuations in defect energetics are significantly smaller, only  $\approx 0.2$  eV. Here, it is important to note that the PBE calculations of lead-based HaPs benefit from a fortuitous cancelation of errors, namely the combination of the PBE underestimate of the gap and the absence of gap closure owing to SOC, to produce a band gap that is close to the experimental results. In GaAs, the effect of SOC on the gap is much less pronounced, and therefore the PBE band gap (0.53 eV) is much smaller than either the experimental GaAs band gap or the HaP band gap. To check whether this affects our conclusions, we performed additional HSE+SOC calculations for selected geometries from the MD run (see SI, section 1, for more details). The band gap then increases to  $\approx 1.3$  eV, which is close to the experimental value, which causes the defect level fluctuation to increase to  $\approx 0.4$  eV. This is larger than what would have been naively expected, but still much smaller than the  $\approx 1$  eV range found for the softer and more anharmonic HaP.

In order to understand the microscopic origins of the unusual fluctuations in the energetics of  $V_{\text{Br}}$  in  $\text{CsPbBr}_3$ , we calculated the correlations of these fluctuations with fluctuations in three other key quantities along the MD trajectory: the CBM, the distance between the two Pb atoms adjacent to the Br vacancy, and the electrostatic energy at either of these two lattice sites, gauged from their calculated  $1s$  core level energy. These results are given in Fig. 2. Clearly, the defect level fluctuations are found to be reasonably correlated with those of the CBM (correlation coefficient: 0.46). However, they are not correlated with fluctuations in the VBM (correlation coefficient: 0.01, see SI, Section 6). This observation is rationalized by the similar chemical nature of the  $n$ -type defect state and the conduction band: The Br vacancy results in dangling  $p$ -orbitals for the two Pb atoms surrounding it, and the conduction band also comprises Pb  $p$ -orbitals. Importantly, the fluctuations in the defect level are also highly correlated with fluctuations in both the distance between the adjacent Pb atoms (correlation

coefficient: 0.72) and the electrostatic potential at these Pb sites (correlation coefficient: 0.56). Significantly weaker correlation (i.e., correlation coefficients smaller than 0.3) was found with fluctuations in other neighboring atoms or the electrostatic potential at their sites. The correlation of the fluctuations in defect energetics with those in the position and potential of the neighboring Pb atoms strongly suggests that nuclear dynamics drive the energy landscape fluctuations which affect the defect energetics.

To gain further insight into the role that Pb atoms may play in the defect energetics, we examined five geometries of the  $V_{\text{Br}}$  defect, selected from the MD trajectory to represent the entire range of defect energy fluctuations. Generally, we found that a smaller Pb-Pb distance is associated with a deeper trap, whereas a larger Pb-Pb distance is associated with a shallower one. In Fig. 3a, the geometries of the five snapshots are overlaid, showing that strong Pb motion is indeed a dominant geometrical feature in the vicinity of the defect. Fig. 3b then shows the band charge density associated with the defect state for the five snapshots. Clearly, deeper defect energies (smaller Pb-Pb distances) are associated with localization of the defect state, whereas shallower defect states (larger Pb-Pb distances) are more delocalized. This can be rationalized by considering that a larger overlap of the dangling Pb  $p$ -orbitals, which is of course related to the Pb-Pb distance, pushes the defect state into the gap. This interpretation is further supported by MD runs for the supercell containing a positively charged Br vacancy (see SI, Section 7, for details). While the overall findings are similar to the case of the neutral species, and the width of the energy fluctuations of the defect level is still very large, it only amounts to about half that of the neutral defect. This makes sense if one considers that the removal of an electron creates more repulsion between the positively charged Pb atoms and limits their range of motion to areas farther away from the vacancy. This reduced range of motion then translates to reduced fluctuations in the energy of the defect state.

These results, for both charge states of the defect, leave us with one very important insight – defect energetics in HaPs are dynamic. Therefore, pinning down a particular unique static value, even if highly precise, is not sufficiently informative. The strong spatial and temporal modulation of the energetics in HaPs is *dictated by the local and instantaneous arrangement of atoms rather than by one global static geometry*, causing the defect energetics to span half of the forbidden band gap on the ps time scale. This effect has been demonstrated here for the case of the  $V_{\text{Br}}$  defect in  $\text{CsPbBr}_3$ , which is an abundant defect in HaP. The situation may well be similar for other types of defects

in view of the soft HaP lattice. Of course, each defect should be studied individually, but the large defect-level fluctuations found in our example are fundamentally incompatible with the static picture and suffice to establish that it cannot be taken for granted *a priori*.

Our results may have important implications for future studies on HaPs as well as potential ramifications for devices. This is because the time scale of the defect energy fluctuations implies a frequency dependence in the response to measurements probing the defect characteristics of HaPs. This poses significant challenges also to experimental defect characterization of HaPs, where analysis of the raw experimental data often assumes a well-defined energy level over long time scales. Finally, we hypothesize that defect fluctuations could facilitate a new mechanism for defect tolerance: While the average defect energy position may be deep in the gap and thus likely to capture charge carriers and harmful for solar cell operation, the MD-DFT results imply that the structural fluctuations of the environment can also lead to frequent visits to regions of shallow defect energies. These are less likely to trap carriers, but could release captured ones, which could potentially mitigate deleterious trapping effects of the defect. We believe that the results presented in this work call for further study of this possibility.

In conclusion, we have considered the case of the Br vacancy in CsPbBr<sub>3</sub> as a prototype for examining the impact of pertinent nuclear fluctuations at RT on defect energetics in HaPs. Our DFT-MD results show that the static picture of defects breaks down in CsPbBr<sub>3</sub>: the energy of the  $V_{\text{Br}}$  level is dynamic and oscillates widely within the forbidden band gap, which is unusual compared to conventional semiconductors such as GaAs. The energy fluctuations of the defect state were found to be correlated with the distance of neighboring Pb atoms as well as with the surrounding electrostatic potential. Therefore, the massive energy fluctuations of the  $V_{\text{Br}}$  defect in CsPbBr<sub>3</sub> are dictated by the large-amplitude nuclear displacements of the HaP lattice. These findings bear important implications for future experimental and theoretical studies on defect characteristics of HaPs, as well as their consequences in devices, and may specifically assist defect tolerance in these materials.

## Acknowledgements

AVC and LK acknowledge support by the Minerva Foundation. DAE acknowledges funding provided by the Alexander von Humboldt Foundation in the framework of the Sofja Kovalevskaja Award endowed by the German Federal Ministry of Education and Research is acknowledged. AMR acknowledges support from the US National Science Foundation, under grant DMR-1719353. Computing time granted by the John von Neumann Institute for Computing (NIC) and provided on the supercomputer JURECA<sup>91</sup> at the Jülich Supercomputing Centre (JSC) is appreciated as well.

## References

1. Li, W. *et al.* Chemically diverse and multifunctional hybrid organic-inorganic perovskites. *Nat. Rev. Mater.* **2**, 16099 (2017).
2. Ono, L. K., Juarez-Perez, E. J. & Qi, Y. Progress on Perovskite Materials and Solar Cells with Mixed Cations and Halide Anions. *ACS Applied Materials and Interfaces* **9**, 30197–30246 (2017).
3. Ahmadi, M., Wu, T. & Hu, B. A Review on Organic–Inorganic Halide Perovskite Photodetectors: Device Engineering and Fundamental Physics. *Advanced Materials* **29**, 1605242 (2017).
4. Correa-Baena, J. P. *et al.* Promises and challenges of perovskite solar cells. *Science* **358**, 739–744 (2017).
5. Kovalenko, M. V., Protesescu, L. & Bodnarchuk, M. I. Properties and potential optoelectronic applications of lead halide perovskite nanocrystals. *Science* **358**, 745–750 (2017).
6. Van Le, Q., Jang, H. W. & Kim, S. Y. Recent Advances toward High-Efficiency Halide Perovskite Light-Emitting Diodes: Review and Perspective. *Small Methods* 1700419 (2018).
7. Leijtens, T., Bush, K. A., Prasanna, R. & McGehee, M. D. Opportunities and challenges for tandem solar cells using metal halide perovskite semiconductors. *Nature Energy* **3**, 1–11 (2018).
8. Brenner, T. M., Egger, D. A., Kronik, L., Hodes, G. & Cahen, D. Hybrid organic - Inorganic perovskites: Low-cost semiconductors with intriguing charge-transport properties. *Nat. Rev. Mater.* **1**, 15007 (2016).
9. Stranks, S. D. *et al.* Electron-Hole Diffusion Lengths Exceeding 1 Micrometer

- in an Organometal Trihalide Perovskite Absorber. *Science* **342**, 341–344 (2018).
10. Wehrenfennig, C., Eperon, G. E., Johnston, M. B., Snaith, H. J. & Herz, L. M. High charge carrier mobilities and lifetimes in organolead trihalide perovskites. *Adv. Mater.* **26**, 1584–1589 (2014).
  11. Shi, D. *et al.* Low trap-state density and long carrier diffusion in organolead trihalide perovskite single crystals. *Science* **347**, 519–522 (2015).
  12. Selcuk, H., Sene, J. J., Sarikaya, H. Z., Bekbolet, M. & Anderson, M. A. An innovative photocatalytic technology in the treatment of river water containing humic substances. *Water Sci. Technol.* **49**, 153–158 (2004).
  13. Zhao, Y. & Zhu, K. Solution chemistry engineering toward high-efficiency perovskite solar cells. *J. Phys. Chem. Lett.* **5**, 4175–4186 (2014).
  14. Yan, K. *et al.* Hybrid Halide Perovskite Solar Cell Precursors: Colloidal Chemistry and Coordination Engineering behind Device Processing for High Efficiency. *J. Am. Chem. Soc.* **137**, 4460–4468 (2015).
  15. Saffarian, P., Najar Peeraye, S., Amani, J. & Imani Fooladi, A. A. Evaluation of the expression of recombinant type a botulinum neurotoxin light chain loaded onto a cell-penetrating peptide. *J. Babol Univ. Med. Sci.* **18**, 25–30 (2016).
  16. Stranks, S. D., Nayak, P. K., Zhang, W., Stergiopoulos, T. & Snaith, H. J. Formation of thin films of organic-inorganic perovskites for high-efficiency solar cells. *Angew. Chemie - Int. Ed.* **54**, 3240–3248 (2015).
  17. Rosenberg, J. W., Legodi, M. J., Rakita, Y., Cahen, D. & Diale, M. Laplace current deep level transient spectroscopy measurements of defect states in methylammonium lead bromide single crystals. *J. Appl. Phys.* **122**, 145701 (2017).
  18. Xing, G. *et al.* Low-temperature solution-processed wavelength-tunable perovskites for lasing. *Nat. Mater.* **13**, 476–480 (2014).
  19. Kirchartz, T., Markvart, T., Rau, U. & Egger, D. A. Impact of Small Phonon Energies on the Charge-Carrier Lifetimes in Metal-Halide Perovskites. *J. Phys. Chem. Lett.* **9**, 939–946 (2018).
  20. Brandt, R. E., Stevanović, V., Ginley, D. S. & Buonassisi, T. Identifying defect-tolerant semiconductors with high minority-carrier lifetimes: Beyond hybrid lead halide perovskites. *MRS Commun.* **5**, 265–275 (2015).
  21. Egger, D. A. *et al.* What Remains Unexplained about the Properties of Halide Perovskites? *Adv. Mater.* **30**, 1–11 (2018).

22. Buin, A. *et al.* Materials processing routes to trap-free halide perovskites. *Nano Lett.* **14**, 6281–6286 (2014).
23. Du, M. H. Efficient carrier transport in halide perovskites: Theoretical perspectives. *J. Mater. Chem. A* **2**, 9091–9098 (2014).
24. Xiao, Z., Zhou, Y., Hosono, H. & Kamiya, T. Intrinsic defects in a photovoltaic perovskite variant  $\text{Cs}_2\text{SnI}_6$ . *Phys. Chem. Chem. Phys.* **17**, 18900–18903 (2015).
25. Yang, J. H., Yin, W. J., Park, J. S. & Wei, S. H. Self-regulation of charged defect compensation and formation energy pinning in semiconductors. *Sci. Rep.* **5**, 16977 (2015).
26. Du, M. H. Density functional calculations of native defects in  $\text{CH}_3\text{NH}_3\text{PbI}_3$ : Effects of spin - Orbit coupling and self-interaction error. *J. Phys. Chem. Lett.* **6**, 1461–1466 (2015).
27. Shi, T., Yin, W. J., Hong, F., Zhu, K. & Yan, Y. Unipolar self-doping behavior in perovskite  $\text{CH}_3\text{NH}_3\text{PbBr}_3$ . *Appl. Phys. Lett.* **106**, 3–8 (2015).
28. Walsh, A., Scanlon, D. O., Chen, S., Gong, X. G. & Wei, S. H. Self-regulation mechanism for charged point defects in hybrid halide perovskites. *Angew. Chemie - Int. Ed.* **54**, 1791–1794 (2015).
29. Kim, J., Chung, C. H. & Hong, K. H. Understanding of the formation of shallow level defects from the intrinsic defects of lead tri-halide perovskites. *Phys. Chem. Chem. Phys.* **18**, 27143–27147 (2016).
30. Mosconi, E., Meggiolaro, D., Snaith, H. J., Stranks, S. D. & De Angelis, F. Light-induced annihilation of Frenkel defects in organo-lead halide perovskites. *Energy Environ. Sci.* **9**, 3180–3187 (2016).
31. Whalley, L. D., Crespo-Otero, R. & Walsh, A. H-Center and V-Center Defects in Hybrid Halide Perovskites. *ACS Energy Lett.* **2**, 2713–2714 (2017).
32. Li, W., Liu, J., Bai, F. Q., Zhang, H. X. & Prezhdo, O. V. Hole Trapping by Iodine Interstitial Defects Decreases Free Carrier Losses in Perovskite Solar Cells: A Time-Domain Ab Initio Study. *ACS Energy Lett.* **2**, 1270–1278 (2017).
33. Liu, N. & Yam, C. Y. First-principles study of intrinsic defects in formamidinium lead triiodide perovskite solar cell absorbers. *Phys. Chem. Chem. Phys.* **20**, 6800–6804 (2018).
34. Kang, J. & Wang, L. W. High Defect Tolerance in Lead Halide Perovskite  $\text{CsPbBr}_3$ . *J. Phys. Chem. Lett.* **8**, 489–493 (2017).
35. Park, J. S., Kim, S., Xie, Z. & Walsh, A. Point defect engineering in thin-film

- solar cells. *Nat. Rev. Mater.* **3**, 194–210 (2018).
36. Yin, J. *et al.* Point Defects and Green Emission in Zero-Dimensional Perovskites. *J. Phys. Chem. Lett.* **9**, 5490–5495 (2018).
  37. Meggiolaro, D. *et al.* Iodine chemistry determines the defect tolerance of lead-halide perovskites. *Energy Environ. Sci.* **11**, 702–713 (2018).
  38. Yin, W. J., Shi, T. & Yan, Y. Unusual defect physics in CH<sub>3</sub>NH<sub>3</sub>PbI<sub>3</sub> perovskite solar cell absorber. *Appl. Phys. Lett.* **104**, 063903/1--063903/4 (2014).
  39. Agiorgousis, M. L., Sun, Y. Y., Zeng, H. & Zhang, S. Strong covalency-induced recombination centers in perovskite solar cell material CH<sub>3</sub>NH<sub>3</sub>PbI<sub>3</sub>. *J. Am. Chem. Soc.* **136**, 14570–14575 (2014).
  40. Wiktor, J., Ambrosio, F. & Pasquarello, A. Mechanism suppressing charge recombination at iodine defects in CH<sub>3</sub>NH<sub>3</sub>PbI<sub>3</sub> by polaron formation. *J. Mater. Chem. A* **6**, 16863–16867 (2018).
  41. Shi, H. & Du, M. H. Shallow halogen vacancies in halide optoelectronic materials. *Phys. Rev. B - Condens. Matter Mater. Phys.* **90**, 1–6 (2014).
  42. Chung, I. *et al.* CsSnI<sub>3</sub>: Semiconductor or metal? High electrical conductivity and strong near-infrared photoluminescence from a single material. High hole mobility and phase-transitions. *J. Am. Chem. Soc.* **134**, 8579–8587 (2012).
  43. Xu, P., Chen, S., Xiang, H. J., Gong, X. G. & Wei, S. H. Influence of defects and synthesis conditions on the photovoltaic performance of perovskite semiconductor CsSnI<sub>3</sub>. *Chem. Mater.* **26**, 6068–6072 (2014).
  44. Freysoldt, C. *et al.* First-principles calculations for point defects in solids. *Rev. Mod. Phys.* **86**, 253–305 (2014).
  45. Chang, Y. H., Park, C. H. & Matsuishi, K. First-Principles Study of the Structural and the Electronic Properties of the Lead-Halide-Based Inorganic-Organic Perovskites (CH<sub>3</sub>NH<sub>3</sub>)PbX<sub>3</sub> and CsPbX<sub>3</sub> (X = Cl, Br, I). *J. Korean Phys. Soc.* **44**, 889–893 (2004).
  46. Feng, J. Mechanical properties of hybrid organic-inorganic CH<sub>3</sub>NH<sub>3</sub>BX<sub>3</sub> (B = Sn, Pb; X = Br, I) perovskites for solar cell absorbers. *APL Mater.* **2**, 81801 (2014).
  47. Rakita, Y., Cohen, S. R., Kedem, N. K., Hodes, G. & Cahen, D. Mechanical properties of APbX<sub>3</sub> (A = Cs or CH<sub>3</sub>NH<sub>3</sub>; X = I or Br) perovskite single crystals. *MRS Commun.* **5**, 623–629 (2015).
  48. Kabakova, I. V. *et al.* The effect of ionic composition on acoustic phonon speeds

- in hybrid perovskites from Brillouin spectroscopy and density functional theory. *J. Mater. Chem. C* **6**, 3861–3868 (2018).
49. Sun, S., Fang, Y., Kieslich, G., White, T. J. & Cheetham, A. K. Mechanical properties of organic-inorganic halide perovskites,  $\text{CH}_3\text{NH}_3\text{PbX}_3$  (X = I, Br and Cl), by nanoindentation. *J. Mater. Chem. A* **3**, 18450–18455 (2015).
  50. Ferreira, A. C. *et al.* Elastic Softness of Hybrid Lead Halide Perovskites. *Phys. Rev. Lett.* **121**, 085502 (2018).
  51. Lee, J.-H., Deng, Z., Bristowe, N. C., Bristowe, P. D. & Cheetham, A. K. The competition between mechanical stability and charge carrier mobility in MA-based hybrid perovskites: insight from DFT. *J. Mater. Chem. C* (2018).
  52. Miyata, K. *et al.* Large polarons in lead halide perovskites. *Sci. Adv.* **3**, 1701217 (2017).
  53. Wu, X. *et al.* Light-induced picosecond rotational disordering of the inorganic sublattice in hybrid perovskites. *Sci. Adv.* **3**, 1602388 (2017).
  54. Maughan, A. E. *et al.* Anharmonicity and Octahedral Tilting in Hybrid Vacancy-Ordered Double Perovskites. *Chem. Mater.* **30**, 472–483 (2018).
  55. Poglitsch, A. & Weber, D. Dynamic disorder in methylammoniumtrihalogenoplumbates (II) observed by millimeter-wave spectroscopy. *J. Chem. Phys.* **87**, 6373–6378 (1987).
  56. Worhatch, R. J., Kim, H. J., Swainson, I. P., Yonkeu, A. L. & Billinge, S. J. L. Study of local structure in selected organic-inorganic perovskites in the  $\text{Pm}\bar{3}\text{m}$  phase. *Chem. Mater.* **20**, 1272–1277 (2008).
  57. Yaffe, O. *et al.* Local Polar Fluctuations in Lead Halide Perovskite Crystals. *Phys. Rev. Lett.* **118**, 136001 (2017).
  58. Motta, C., El-Mellouhi, F. & Sanvito, S. Charge carrier mobility in hybrid halide perovskites. *Sci. Rep.* **5**, 12746 (2015).
  59. Shao, Y. *et al.* Grain boundary dominated ion migration in polycrystalline organic-inorganic halide perovskite films. *Energy Environ. Sci.* **9**, 1752–1759 (2016).
  60. Egger, D. A., Rappe, A. M. & Kronik, L. Hybrid Organic-Inorganic Perovskites on the Move. *Acc. Chem. Res.* **49**, 573–581 (2016).
  61. Beecher, A. N. *et al.* Direct Observation of Dynamic Symmetry Breaking above Room Temperature in Methylammonium Lead Iodide Perovskite. *ACS Energy Lett.* **1**, 880–887 (2016).

62. Sendner, M. *et al.* Optical phonons in methylammonium lead halide perovskites and implications for charge transport. *Mater. Horizons* **3**, 613–620 (2016).
63. Marronnier, A. *et al.* Anharmonicity and Disorder in the Black Phases of Cesium Lead Iodide Used for Stable Inorganic Perovskite Solar Cells. *ACS Nano* **12**, 3477–3486 (2018).
64. Zhang, X., Shen, J. X., Wang, W. & Van De Walle, C. G. First-Principles Analysis of Radiative Recombination in Lead-Halide Perovskites. *ACS Energy Lett.* **3**, 2329–2334 (2018).
65. Motta, C. *et al.* Revealing the role of organic cations in hybrid halide perovskite CH<sub>3</sub>NH<sub>3</sub>PbI<sub>3</sub>. *Nat. Commun.* **6**, 7026 (2015).
66. Carignano, M. A., Kachmar, A. & Hutter, J. Thermal effects on CH<sub>3</sub>NH<sub>3</sub>PbI<sub>3</sub> perovskite from Ab initio molecular dynamics simulations. *J. Phys. Chem. C* **119**, 8991–8997 (2015).
67. Bechtel, J. S. & Van der Ven, A. Octahedral tilting instabilities in inorganic halide perovskites. *Phys. Rev. Mater.* **2**, 025401 (2018).
68. Schueller, E. C. *et al.* Crystal Structure Evolution and Notable Thermal Expansion in Hybrid Perovskites Formamidinium Tin Iodide and Formamidinium Lead Bromide. *Inorg. Chem.* **57**, 695–701 (2018).
69. Fabini, D. H. *et al.* Universal Dynamics of Molecular Reorientation in Hybrid Lead Iodide Perovskites. *J. Am. Chem. Soc.* **139**, 16875–16884 (2017).
70. Capitani, F. *et al.* Locking of Methylammonium by Pressure-Enhanced H-Bonding in (CH<sub>3</sub>NH<sub>3</sub>)PbBr<sub>3</sub> Hybrid Perovskite. *J. Phys. Chem. C* **121**, 28125–28131 (2017).
71. Uratani, H. & Yamashita, K. Inorganic Lattice Fluctuation Induces Charge Separation in Lead Iodide Perovskites: Theoretical Insights. *J. Phys. Chem. C* **121**, 26648–26654 (2017).
72. Yang, R. X., Skelton, J. M., Da Silva, E. L., Frost, J. M. & Walsh, A. Spontaneous octahedral tilting in the cubic inorganic cesium halide perovskites CsSnX<sub>3</sub> and CsPbX<sub>3</sub> (X = F, Cl, Br, I). *J. Phys. Chem. Lett.* **8**, 4720–4726 (2017).
73. Guo, Y. *et al.* Interplay between organic cations and inorganic framework and incommensurability in hybrid lead-halide perovskite CH<sub>3</sub>NH<sub>3</sub>PbBr<sub>3</sub>. *Phys. Rev. Mater.* **1**, 042401 (2017).
74. Perdew, J. P., Burke, K. & Ernzerhof, M. Generalized gradient approximation made simple. *Phys. Rev. Lett.* **77**, 3865–3868 (1996).

75. Tkatchenko, A. & Scheffler, M. Accurate molecular van der Waals interactions from ground-state electron density and free-atom reference data. *Phys. Rev. Lett.* **102**, 073005 (2009).
76. Bučko, T., Lebègue, S., Hafner, J. & Ángyán, J. G. Improved density dependent correction for the description of London dispersion forces. *J. Chem. Theory Comput.* **9**, 4293–4299 (2013).
77. Bučko, T., Lebègue, S., Ángyán, J. G. & Hafner, J. Extending the applicability of the Tkatchenko-Scheffler dispersion correction via iterative Hirshfeld partitioning. *J. Chem. Phys.* **141**, 0–17 (2014).
78. Heyd, J., Scuseria, G. E. & Ernzerhof, M. Hybrid functionals based on a screened Coulomb potential. *J. Chem. Phys.* **118**, 8207–8215 (2003).
79. Kresse, G. & Furthmüller, J. Efficient iterative schemes for ab initio total-energy calculations using a plane-wave basis set. *Phys. Rev. B - Condens. Matter Mater. Phys.* **54**, 11169–11186 (1996).
80. Joubert, D. From ultrasoft pseudopotentials to the projector augmented-wave method. *Phys. Rev. B - Condens. Matter Mater. Phys.* **59**, 1758–1775 (1999).
81. Egger, D. A. & Kronik, L. Role of dispersive interactions in determining structural properties of organic-inorganic halide perovskites: Insights from first-principles calculations. *J. Phys. Chem. Lett.* **5**, 2728–2733 (2014).
82. Li, J. & Rinke, P. Atomic structure of metal-halide perovskites from first principles: The chicken-and-egg paradox of the organic-inorganic interaction. *Phys. Rev. B* **045201**, 12 (2016).
83. Wang, Y. *et al.* Density functional theory analysis of structural and electronic properties of orthorhombic perovskite  $\text{CH}_3\text{NH}_3\text{PbI}_3$ . *Phys. Chem. Chem. Phys.* **16**, 1424–1429 (2014).
84. Beck, H., Gehrman, C. & Egger, D. A. Structure and Binding in Halide Perovskites: Analysis of Static and Dynamic Effects from Dispersion-Corrected Density Functional Theory. ArXiv:1901.08820 (2019).
85. Stoumpos, C. C. *et al.* Crystal growth of the perovskite semiconductor  $\text{CsPbBr}_3$ : A new material for high-energy radiation detection. *Cryst. Growth Des.* **13**, 2722–2727 (2013).
86. Nosé, S. A unified formulation of the constant temperature molecular dynamics methods. *J. Chem. Phys.* **81**, 511–519 (1984).
87. Hoover, W. G. Constant-pressure equations of motion. *Phys. Rev. A* **34**, 2499–

- 2500 (1986).
88. Jones, R. O. & Gunnarsson, O. The density functional formalism, its applications and prospects. *Rev. Mod. Phys.* **61**, 689–746 (1989).
  89. Mladenović, M. & Vukmirović, N. Effects of thermal disorder on the electronic structure of halide perovskites: insights from MD simulations. *Phys. Chem. Chem. Phys.* (2018).
  90. Mayers, M., Tan, L. Z., Egger, D. A., Rappe, A. M. & Reichman, D. R. How Lattice and Charge Fluctuations Control Carrier Dynamics in Halide Perovskites. *Nano Lett.* **18**, 8041–8046 (2018).
  91. Krause, D. & Thörnig, P. JURECA: General-purpose supercomputer at Jülich Supercomputing Centre. *J. large-scale Res. Facil. JLSRF* **4**, A132 (2018).

Figures:

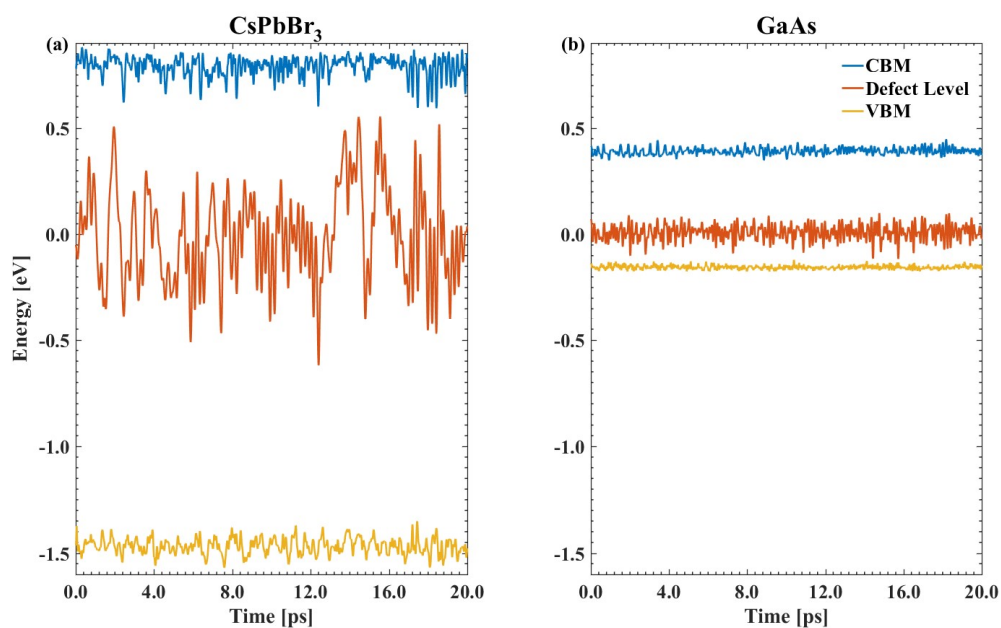


Figure 1: Eigenvalues representing the valence band maximum (VBM), the defect level, and the conduction band minimum (CBM) as a function of time along the MD trajectory, for (a) CsPbBr<sub>3</sub> with a bromine vacancy and (b) GaAs with an As<sub>Ga</sub> anti-site defect. All values are referenced to the average defect level position. The last 20 ps of the MD run of each material are shown.

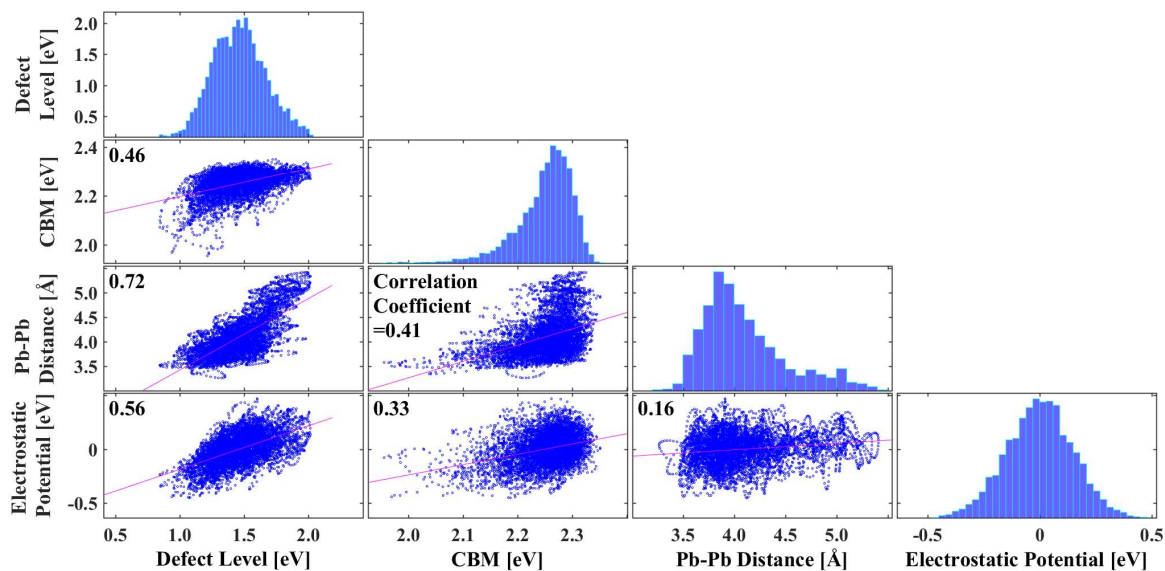


Figure 2: A correlation matrix comparing the fluctuations along the MD trajectory of the defect level, the CBM, the distance between the two Pb atoms that surround the Br vacancy, and the electrostatic potential at these Pb sites. The correlation coefficient between each two variables is given at the upper left corner of the relevant panel. A histogram of each of the variables is given at the upper-most panel of each column. The defect level and CBM values are referenced to the VBM average and the electrostatic potential is referenced to its own average value.

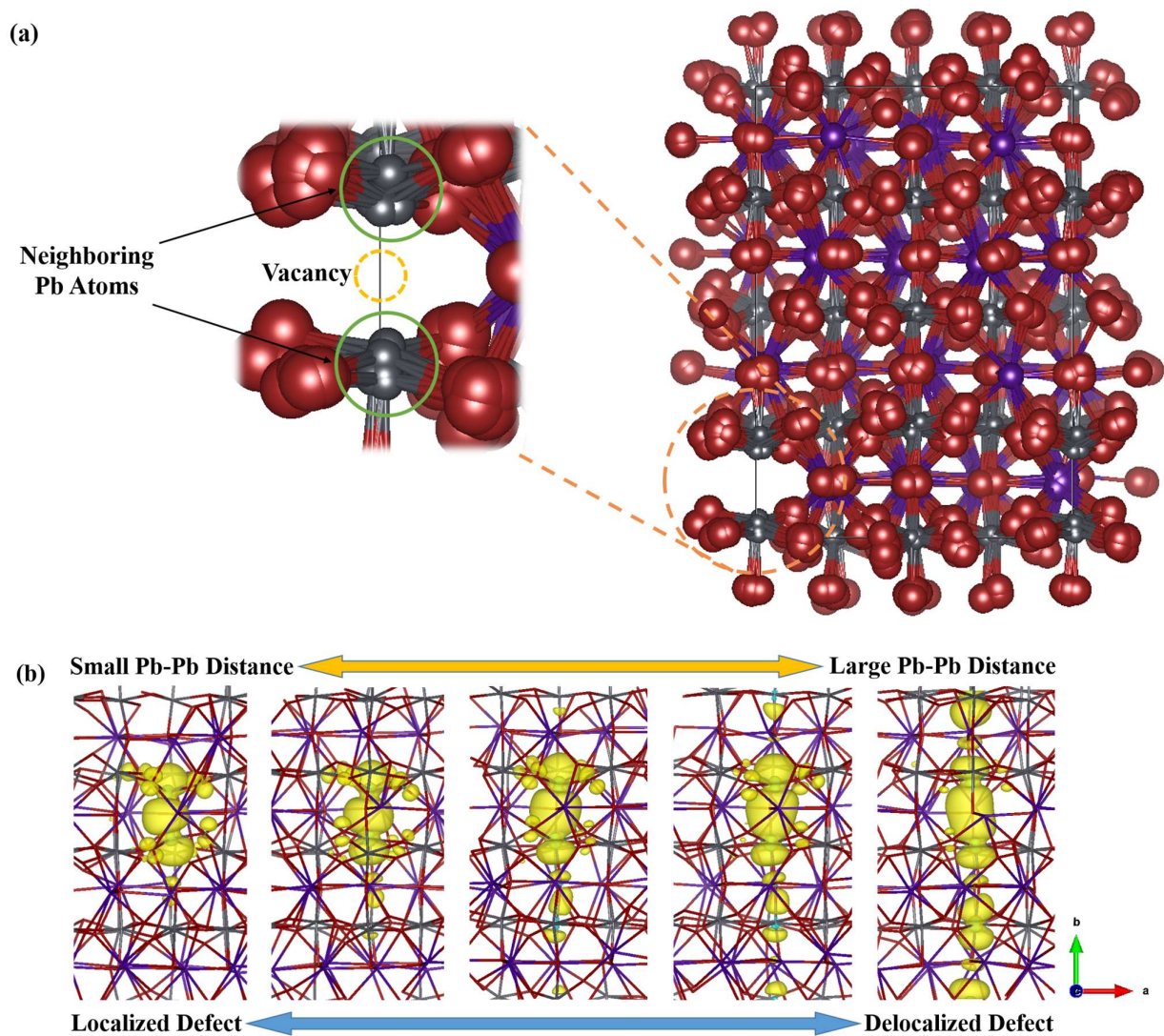


Figure 3: (a) A representation of the dynamic nature of the  $\text{CsPbBr}_3$  system, shown by overlaying five different geometries from the MD trajectory. Cs atoms are in purple, Pb in grey, and Br in red. The location of the vacancy is marked by a yellow dashed circle, and its neighboring Pb atoms are marked by a green circle. (b) The partial charge density of the eigenvalue associated with the defect level (yellow surface), calculated for the same five geometries. The distance between the two Pb atoms that surround the Br vacancy is smallest for the left-most geometry and largest for the right-most geometry. The opposite is true for the amount of charge localization.

**Tables:**

Table 1: Statistical analysis of the eigenvalues representing the VBM, defect level ( $E_d$ ), CBM, and CBM- $E_d$ , performed on the results of the last 30 ps of the MD run of the  $V_{Br}$ -containing  $CsPbBr_3$  supercell.

	<b>VBM [eV]</b>	<b><math>E_d</math> [eV]</b>	<b>CBM [eV]</b>	<b>CBM – <math>E_d</math> [eV]</b>
<b>Minimum</b>	0.49	1.44	2.64	0.25
<b>Maximum</b>	0.73	2.62	2.95	1.29
<b>Range</b>	0.24	1.17	0.31	1.03
<b>Average</b>	0.60	2.06	2.85	0.79
<b>Standard Deviation</b>	0.04	0.21	0.05	0.19